

Flat bands as a route to high-temperature superconductivity in graphite

T.T. Heikkilä and G.E. Volovik

Abstract Superconductivity is traditionally viewed as a low-temperature phenomenon. Within the BCS theory this is understood to result from the fact that the pairing of electrons takes place only close to the usually two-dimensional Fermi surface residing at a finite chemical potential. Because of this, the critical temperature is exponentially suppressed compared to the microscopic energy scales. On the other hand, pairing electrons around a dispersionless (flat) energy band leads to very strong superconductivity, with a mean-field critical temperature linearly proportional to the microscopic coupling constant. The prize to be paid is that flat bands can generally be generated only on surfaces and interfaces, where high-temperature superconductivity would show up. The flat-band character and the low dimensionality also mean that despite the high critical temperature such a superconducting state would be subject to strong fluctuations. Here we discuss the topological and non-topological flat bands discussed in different systems, and show that graphite is a good candidate for showing high-temperature flat-band interface superconductivity.

The purpose of this chapter is to propose a route to increasing the critical temperature of superconductivity by searching for special electronic dispersion that would promote the superconducting strength. We first show that a huge increase in the (mean-field) critical temperature is possible, if a dispersionless energy spectrum, a *flat band* can be created in the system in the absence of the interaction leading to superconducting correlations. We then discuss a few known schemes to generate such (approximate or exact) flat bands.

T.T. Heikkilä

University of Jyväskylä, Department of Physics and Nanoscience Center, P.O. Box 35, FI-40014
University of Jyväskylä, Finland e-mail: Tero.T.Heikkila@jyu.fi

G.E. Volovik

Aalto University, Department of Applied Physics and Low Temperature Laboratory, P.O. Box
15100, FI-00076 AALTO, Finland and L. D. Landau Institute for Theoretical Physics, 117940
Moscow, Russia e-mail: volovik@boojum.hut.fi

1 Superconductivity: pairing energy vs. dispersion

Within the BCS mean-field theory, the occurrence of Cooper pairing at zero temperature can be studied via the free energy density for the pairing energy Δ :

$$F_{\Delta} = -\frac{1}{2} \int \frac{d^d p}{(2\pi\hbar)^d} (E_{\mathbf{p}}(\Delta) - E_{\mathbf{p}}(\Delta = 0)) + \frac{\Delta^2}{2|g|}, \quad (1)$$

where d is the dimensionality, $g < 0$ describes the interaction strength, and $E_{\mathbf{p}}(\Delta) = \sqrt{\varepsilon_{\mathbf{p}}^2 + \Delta^2}$ is the quasiparticle excitation energy at momentum value \mathbf{p} , evaluated in a system with the normal-state dispersion $\varepsilon_{\mathbf{p}}$. The first term in Eq. (1) demonstrates that the formation of a gap Δ decreases the energy of quasiparticles, which fill the negative energy levels of Dirac vacuum. The second term is the cost of the formation of the gap, which perturbs the vacuum. For simplicity, we consider spinless fermions and the gap that does not depend on momentum.

Requiring Δ to minimize F_{Δ} , we get the self-consistency relation

$$\Delta = \frac{|g|}{2} \int \frac{d^d p}{(2\pi\hbar)^d} \frac{\Delta}{E_{\mathbf{p}}(\Delta)}, \quad (2)$$

or

$$1 = \frac{|g|}{2} \int \frac{d^d p}{(2\pi\hbar)^d} \frac{1}{E_{\mathbf{p}}(\Delta)}. \quad (3)$$

Equation (3) dictates the behavior of Δ at different dimensionalities d and for different normal-state energy spectra $\varepsilon_{\mathbf{p}}$.

For s -wave superconductivity in conventional metals with an isotropic Fermi surface and dispersion $\varepsilon = v_F(p - p_F)$ expanded around the Fermi energy $\varepsilon_F = v_F p_F$, the integral in Eq. (3) is concentrated in the vicinity of the Fermi surface

$$1 = \frac{|g|A_d}{(2\pi\hbar)^d v_F} \int_0^{\varepsilon_{\text{uv}}} \frac{d\varepsilon}{\sqrt{\varepsilon^2 + \Delta^2}} \stackrel{\varepsilon_{\text{uv}} \gg \Delta}{\approx} |g|v_F \ln \frac{\varepsilon_{\text{uv}}}{\Delta}. \quad (4)$$

Here $v_F = \frac{A_d}{(2\pi\hbar)^d v_F}$ is the density of states in the normal metal; A_d is the area of the d -dimensional Fermi surface; and $\varepsilon_{\text{uv}} \ll \varepsilon_F$ is the ultraviolet cut-off of the logarithmically diverging integral, such as the Debye temperature. This leads to the exponentially suppressed gap:

$$\Delta = \varepsilon_{\text{uv}} \exp\left(-\frac{1}{|g|v_F}\right), \quad (5)$$

and correspondingly to the exponential suppression of the transition temperature T_c .

Situation drastically changes when the spectrum of the normal state has a flat band – a region in momentum \mathbf{p} where $\varepsilon_{\mathbf{p}} = 0$. Since within the flat band $E_{\mathbf{p}}(\Delta) = \Delta$, Eq. (3) becomes

$$1 = \frac{|g|V_d}{2(2\pi\hbar)^d\Delta}, \quad (6)$$

where V_d is the volume of the flat band in momentum space. Hence instead of the usual exponentially suppressed behavior in Eq. (5) we have the gap Δ that is linearly proportional to the interaction strength:

$$\Delta = \frac{|g|V_d}{2(2\pi\hbar)^d}, \quad (7)$$

Since the critical temperature of the superconductors is typically of the same order of magnitude as the gap at zero temperature, the resulting superconductivity may exist at high temperatures.

It is instructive to consider the intermediate case when the quasiparticle spectrum is

$$\varepsilon(p) = \varepsilon_0 \left(\frac{p}{p_0} \right)^M. \quad (8)$$

Then for $M > d$, Eq. (3) gives the power law dependence of transition temperature on the coupling constant:

$$\Delta \propto |g|^{\frac{M}{M-d}}. \quad (9)$$

In the limit of large $M \gg 1$, the spectrum (8) transforms to the flat band concentrated at $p < p_0$, and the gap (9) asymptotically approaches the linear dependence on the coupling g in Eq. (7). The case with $d = 1$ and $M = 2$, where $\Delta \propto g^2$, has been considered by Kopaev [1] and Kopaev-Rusinov [2].

In the sections below, we consider different systems where the exact or approximate flat bands could be realized.

2 Flat band induced by interaction

2.1 Landau phenomenology

We start with the flat bands induced by interaction between the fermions. As was found by Khodel and Shaginyan [3], the interaction may lead to the merging of different fermionic energy levels, which results in the formation of a dispersionless band, see also Refs. [4, 5]. The effect of the merging of discrete energy levels due to interaction has been reported in a recent paper, Ref. [6].

Their argument is based on the phenomenological Landau's consideration on the derivation of the distribution function $n_{\mathbf{p}}$ of fermions at $T = 0$. It is determined by the energy functional $\mathcal{E}\{n(\mathbf{p})\}$, whose variational derivative $\varepsilon_{\mathbf{p}}$ is the quasiparticle energy. The variation of this functional gives the equation for $n_{\mathbf{p}}$ and $\varepsilon_{\mathbf{p}}$:

$$\delta\mathcal{E}\{n(\mathbf{p})\} = \int \frac{d^d p}{(2\pi\hbar)^d} \varepsilon_{\mathbf{p}} \delta n_{\mathbf{p}} = 0. \quad (10)$$

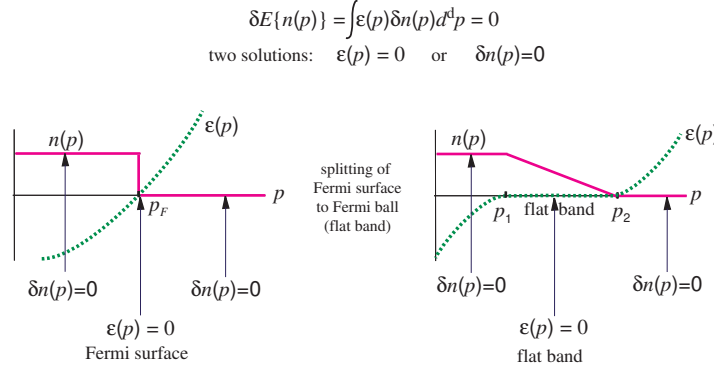


Fig. 1 Illustration of the formation of the Khodel-Shaginyan flat band due to interaction between fermions. (*Top*): the Landau model of the Fermi liquid considers the energy $\mathcal{E}\{n(\mathbf{p})\}$ as the functional of the distribution function $n(\mathbf{p})$ of quasiparticles. The variation of the functional gives two types of solutions: $\varepsilon_{\mathbf{p}} = 0$ or $\delta n_{\mathbf{p}} = 0$. (*Left*): distribution of quasiparticles in the class of Fermi liquids. Two regions with solutions $\delta n_{\mathbf{p}} = 0$ are separated by the surface with solution $\varepsilon_{\mathbf{p}} = 0$. This is the Fermi surface. Topological stability of this class is demonstrated in Fig. 2. (*Right*): For strong interaction (large interaction constant), the intermediate region with the solution $\varepsilon_{\mathbf{p}} = 0$, may become finite. This is the flat band. Topological structure of such flat band is demonstrated in Fig. 3.

Since the quasiparticle distribution function is constrained by the Pauli principle $0 \leq n_{\mathbf{p}} \leq 1$, there are two classes of solutions of the variational problem. One class is $\varepsilon_{\mathbf{p}} = 0$, which is valid if $0 < n_{\mathbf{p}} < 1$; another one is $\delta n_{\mathbf{p}} = 0$ with $n_{\mathbf{p}} = 0$ or $n_{\mathbf{p}} = 1$. In the following we illustrate these two classes of solutions.

2.2 Landau Fermi liquid and its topological stability

Let us start with the Fermi gas – the system of free fermions with the spectrum $\varepsilon_{\mathbf{p}} = p^2/2m - \mu$, where $\mu > 0$. The energy functional for free fermions is $\mathcal{E}\{n(\mathbf{p})\} = \int \frac{d^d p}{(2\pi\hbar)^d} \varepsilon_{\mathbf{p}} n_{\mathbf{p}}$, which gives the solution shown in Fig. 1 (*left*). The solution of the class $\varepsilon_{\mathbf{p}} = 0$ forms the Fermi surface with radius p_F , where $p_F^2/2m = \mu$. Outside of the Fermi surface the distribution function $n_{\mathbf{p}} = \text{const}$, with $n_{\mathbf{p}} = 1$ for $p < p_F$ and $n_{\mathbf{p}} = 0$ for $p > p_F$. This corresponds to the class of solutions with $\delta n_{\mathbf{p}} = 0$.

The structure with the Fermi surface is topologically protected. The topological stability can be illustrated using the $d = 2$ system, when the Fermi surface $p = p_F$ is the 1d circle. For that one has to consider the Green's function at imaginary frequency:

$$G(\omega, \mathbf{p}) = \frac{1}{i\omega - \left(\frac{p^2}{2m} - \mu\right)}. \quad (11)$$

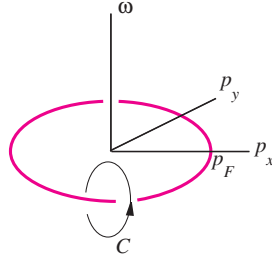


Fig. 2 Illustration of the topological stability of the Fermi surface on an example case with dimension $d = 2$, when the Fermi surface forms a closed loop. Green's function has singularities on the line $\omega = 0$, $p_x^2 + p_y^2 = p_F^2$ in the three-dimensional space (ω, p_x, p_y) . Stability of the Fermi surface is protected by the invariant (12) which is represented by an integral over an arbitrary contour C around the Green's function singularity.

The Green's function in Eq. (11) has singularities at $\omega = 0$ for \mathbf{p} belonging to the Fermi surface. These points form a closed line in the three dimensional (ω, p_x, p_y) -space, see Fig. 2 for $d = 2$. This line has a topological winding number: the phase Φ of the Green's function, $G = |G|e^{\Phi}$ changes by 2π along an arbitrary contour C around the line. In other words, the Fermi surface represents the p -space analog of the vortex lines in superfluids and superconductors, where the phase of the order parameter changes by 2π around the vortex. The 2π winding of the phase Φ cannot change under small deformations of the parameters of the system, and thus is robust to the interactions between the particles, if we do not consider the superconducting, magnetic or other phase transition, which drastically (non-perturbatively) reconstructs the energy spectrum. This topological stability is the reason why interacting Fermi liquids preserve the Fermi surface.

For more complicated cases, when the Green's function has spin, band and other indices, and for arbitrary dimension d the winding number N of the Fermi surface is expressed analytically in terms of the matrix Green's function in the following form:

$$N = \text{tr} \oint_C \frac{dl}{2\pi i} G(\omega, \mathbf{p}) \partial_l G^{-1}(\omega, \mathbf{p}). \quad (12)$$

Here the integral is taken over an arbitrary contour C around the Green's function singularity in the $d + 1$ momentum-frequency space. For the Green's function in Eq. (11) the topological invariant $N = 1$.

2.3 Khodel-Shaginyan flat band and its topology

When the interaction between the particles is strong enough, so that it starts dominating over the fermionic statistics, a more classical behavior of the distribution function may emerge, in which the natural solution of the variational problem corre-

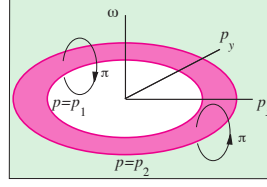


Fig. 3 Illustration of the topological structure of the Khodel-Shaginyan flat band in a $d = 2$ system. According to Fig. 1 (*right*) the Fermi surface at $p = p_F$ spreads into a flat band concentrated in the region $p_1 < p < p_2$. Correspondingly the line of the Green's function singularities in Fig. 2 – a vortex line – is spreading to an analog of a domain wall terminating on a pair of π -vortices at $p = p_1$ and $p = p_2$. [4]

sponds to a zero value of the variational derivative, $\delta \mathcal{E}\{n(\mathbf{p})\}/\delta n_{\mathbf{p}} = 0$. Therefore, with an increasing interaction strength one may expect the topological quantum phase transition to the distribution in Fig. 1 (*right*), where the solution $\varepsilon_{\mathbf{p}} = 0$ is spread over a finite region in momentum space, i.e., forming a flat band.

The topological structure of the Khodel-Shaginyan flat band is shown in Fig. 3. The vortex line with 2π winding transforms to the domain wall, at which the Green's function has a jump, $G(\omega = +0, p_x, p_y) - G(\omega = -0, p_x, p_y) \neq 0$. This domain wall terminates on π vortices.

2.4 Flat band near the saddle point

Here we consider the formation of the Khodel-Shaginyan flat band in the vicinity of a saddle point in the $d = 2$ quasiparticle spectrum using the phenomenological Landau theory [7] and compare it with the results of numerical simulations of the Hubbard model [8].

The simple Landau-type functional for the interacting Fermi liquid is

$$\mathcal{E}\{n(\mathbf{p})\} = \sum_{\mathbf{p}} n_{\mathbf{p}} \varepsilon_{\mathbf{p}}^{(0)} + \frac{1}{2} \sum_{\mathbf{p}, \mathbf{p}'} f(\mathbf{p}, \mathbf{p}') n_{\mathbf{p}} n_{\mathbf{p}'}. \quad (13)$$

We illustrate the flat band solution using an even simpler functional with contact interaction:

$$\mathcal{E}\{n(\mathbf{p})\} = \sum_{\mathbf{p}} \left[\varepsilon_{\mathbf{p}}^{(0)} n_{\mathbf{p}} + \frac{1}{2} U \left(n_{\mathbf{p}} - \frac{1}{2} \right)^2 \right], \quad (14)$$

where $U > 0$. This functional has always a flat band solution with $0 < n_{\mathbf{p}} < 1$:

$$\varepsilon_{\mathbf{p}} = \frac{\delta \mathcal{E}}{\delta n_{\mathbf{p}}} = \varepsilon_{\mathbf{p}}^{(0)} + U \left(n_{\mathbf{p}} - \frac{1}{2} \right) = 0, \quad (15)$$

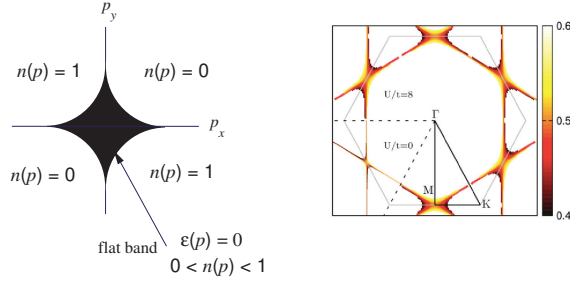


Fig. 4 Flat band emerging near a saddle point. (*Left*): from the simplified Landau-type theory in Eqs. (14)-(16) with $\mu = 0$. The flat band is concentrated in the black region. (*Right*): from the numerical solution of the Hubbard model [8] [D. Yudin, *et al.*, Phys. Rev. Lett. **112**, 070403 (2014)], showing the spectral function within the reciprocal space of an interacting triangular lattice. The lower left sextant corresponds to the noninteracting case $U = 0$. For large U the band flattening is clearly seen near the saddle points.

$$n_{\mathbf{p}} = \frac{1}{2} - \frac{\epsilon_{\mathbf{p}}^{(0)}}{U}, \quad 0 < n_{\mathbf{p}} < 1. \quad (16)$$

In the vicinity of the saddle point the non-perturbed spectrum (i.e. at $U = 0$) has the form $\epsilon_{\mathbf{p}}^{(0)} = \frac{p_x p_y}{m} - \mu$. For $\mu \neq 0$, there are two hyperbolic Fermi surfaces. They interconnect at the Lifshitz transition, which takes place at $\mu = 0$. When the interaction U is switched on, the flat bands emerge. Figure 4 (*left*) demonstrates the flat band at $\mu = 0$. The same shape of the region with the flat band has been obtained from the numerical simulations of the Hubbard model [8], see Fig. 4 (*right*).

3 Flat bands in topological semimetals

In the previous section we discuss the fermion condensate – the flat band, which may emerge due to interactions in the vicinity of a singularity in the non-interacting spectrum. There are also other ways to generate flat bands or approximate flat bands. Historically the flat bands first appeared as Landau levels of charged particles in a magnetic field [9]. Here we discuss the flat bands that have purely topological origin. They may exist without a magnetic field, and they are not very sensitive to interactions. The flat band may emerge as the surface or interface state in topological semimetals [10, 11, 12], which we discuss in this section. The flat band may also appear at the strained interfaces with misfit dislocations, which play the role of effective magnetic field. Such flat bands are discussed in Sec. 4.

In this section we characterize semimetals that have an internal spin-like structure. All the examples discussed here can be characterized via the topological invariant of the form [13]

$$N_1 = \text{tr} \oint_C \frac{d\mathbf{l}}{4\pi i} \cdot [\Gamma H^{-1}(\mathbf{p}) \partial_l H(\mathbf{p})], \quad (17)$$

where H is the Hamiltonian in the momentum space; Γ is a matrix which commutes or anti-commutes with the Hamiltonian, such as the third Pauli matrix σ_3 acting on the spin-like degree of freedom; and C is a contour in momentum space, specified separately for each semimetal.

In semimetals, the flat bands are realized as a particular consequence of the bulk-boundary correspondence of topological media (see [14, 15, 16] or Sec. 22.1 in [17]). If for example a 3D bulk system contains Weyl points, then an interface with a topologically trivial material, or with a material having a different value of topological invariants contains a line of zeroes – the Fermi arc [18]. The termination points of the Fermi arc are given by projections of the Weyl points to the interface. In the same manner the Dirac lines in 3D bulk or Dirac points in 2D bulk give rise to the nodes of higher dimension at the interface – the flat band [10, 11, 12]. The boundaries of the flat band are determined by the projection of the Dirac line or Dirac points to the interface.

3.1 Topological nodes: Dirac lines and Dirac points

Let us consider an example semimetal characterized by an even number of 2-dimensional Dirac points, such as that found in graphene around the two valleys. Close to the Dirac point the Hamiltonian can be written as a 2×2 matrix in (pseudo)spin space,

$$H = v_F \begin{pmatrix} 0 & p_x - ip_y \\ p_x + ip_y & 0 \end{pmatrix} = v_F \mathbf{p} \cdot \boldsymbol{\sigma}, \quad (18)$$

where $\mathbf{p} = (p_x, p_y)$ and $\boldsymbol{\sigma} = (\sigma_x, \sigma_y)$, where σ_j are Pauli matrices. The eigenvalues of H satisfy $\varepsilon^2 = v_F^2 |p|^2$ having a node $\varepsilon(\mathbf{p} = 0)$ in a single point in momentum space. To illustrate the topological protection of this node, let us add a perturbation of the form $V(\mathbf{p}) = \mathbf{v}(\mathbf{p}) \cdot \boldsymbol{\sigma}$, where $\mathbf{v} = (v_x, v_y)$ does not break the (pseudo)spin symmetry. As a result, the dispersion becomes $\varepsilon^2 = (v_F p_x + v_x)^2 + (v_F p_y + v_y)^2$, which again has a single node at $(p_x, p_y) = -(v_x, v_y)/v_F$. The only effect of the potential is thus to shift the node, but not annihilate it. This property can be expressed via the presence of the topological charge of the form (17), where $\Gamma = \sigma_z$ and the contour C goes around the Dirac point in the 2D momentum space (see Fig. 5). For the Hamiltonian in Eq. (18), we get $N_1 = 1$. In graphene, there are two Dirac points: the first one has the form in Eq. (18), and the second is otherwise the same but $p_y \mapsto -p_y$. In that case the second Dirac point has $N_1 = -1$. These topological charges stay invariant to perturbations of the form $V(\mathbf{p})$, as long as we shift the contour of integration along with the shift of the Dirac point, and as long as the two nodes do not merge due to such a perturbation.

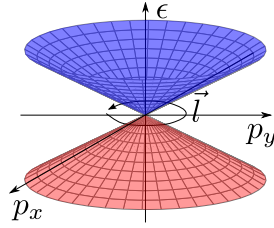


Fig. 5 2D Dirac/Fermi point in momentum space and the line of integration for the topological invariant N_1 .

In 3D materials, the topological charge in Eq. (17) characterizes lines of nodes – the Dirac lines. The Dirac lines are readily obtained in superfluids and superconductors, where the symmetry operator Γ contains the particle-hole symmetry. In particular, the Dirac line exists in the polar phase of superfluid ^3He [19] and may appear in superconductors without inversion symmetry [12]. The topologically stable Dirac lines give rise to the topologically protected surface flat band. According to the bulk-surface correspondence, the boundary of the flat band is determined by the projection of the nodal line on to surfaces. In nonsuperconducting materials the corresponding symmetry which enters Eq. (17) can be only approximate, being violated by spin-orbit interaction, or by the higher order hopping elements. This leads to formation of approximately flat surface bands as it happens for example in graphite [20], graphene networks [21] and possibly in some other materials [22].

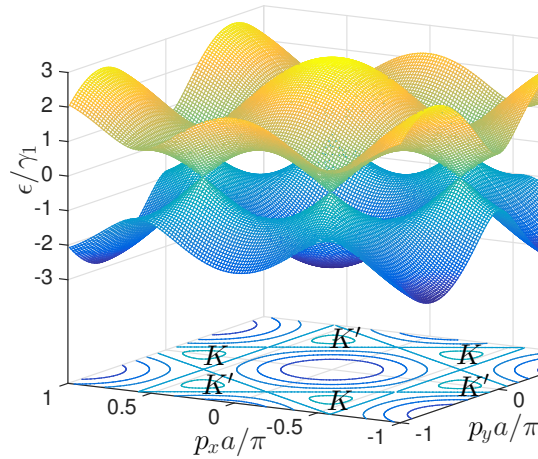


Fig. 6 Energy spectrum in the conduction and valence bands of graphene. Here a is the lattice constant, and γ_1 denotes the nearest-neighbour hopping parameter in the tight-binding lattice. The underlying contour plot shows the positions of the Dirac points. Only two of these points are non-equivalent, the others are connected via reciprocal lattice vectors.

We first consider the case of graphene, whose energy spectrum within the valence and conduction bands is plotted in Fig. 6. This spectrum follows for example from the nearest-neighbour tight-binding model on a honeycomb lattice, see [23, 24]. Around the specific points, marked K and K' in the figure, the low-energy Hamiltonian is of the form of Eq. (18). These points are described by the topological charge N_1 , such that $N_1(K) = +1$ and $N_1(K') = -1$.

Figure 7 shows the formation of flat bands at the edges of graphene [10]. There, we show the locations of the K and K' points in the 2d momentum plane, and consider the presence of an edge placed in the x -direction. Now, the edge marks a boundary between graphene, which is a nodal semimetal, and vacuum, which is a trivial insulator. By the bulk-boundary correspondence we may hence expect flat band states at the edge. Since we maintain translational invariance along the x direction, p_x remains a good quantum number and it also parametrizes the edge states and their dispersion $\epsilon_e(p_x)$. According to the bulk-boundary correspondence, the projections of the Dirac points to the boundary determine the end points of the flat band. From Fig. 7 it is clear that the termination points of the flat band must be located at p_x values corresponding to the p_x -component of the K and K' points. When p_x crosses these points, the normal to the interface run across either K or K' points and the topological invariant in Eq. (17) along the normal changes. However, from the figure alone one cannot say which of the regions between the K and K' points contain flat bands and which not. The solution is to construct the system by repeating a set of infinite chains, and construct the topological invariant, in this case called the Zak phase [25] for these chains. As shown for example in [25, 10], the details of this procedure depend on the microscopic form of the edge, which is either of the “bearded” or the “zigzag” type. Figure 7 illustrates the resulting positions of the flat band dispersion in momentum space.

If we were to place the interface in the y direction (in which case we would obtain the “armchair” edge), there would be no flat band due to the fact that the normal to the interface would run across both K and K' points. In this case the change of the topological charge across this normal line would be $N_1(K) + N_1(K') = 0$.

In the following sections we explain the topological invariants in multilayer graphene structures and discuss the consequent (approximate) flat band surface states.

3.2 *From graphene to graphite*

In graphite, the coupling between the graphene layers is much weaker than that within the atoms producing the hexagonal lattice in individual layers. Because of this, we may assume that the individual layers remain to be described by the two-dimensional low-energy momentum-space Hamiltonian of the form in Eq. (18). In the (most stable) AB stacking, the pair of layers is arranged so that the graphene hexagons are rotated with respect to each other by 30° . As a result, one pair of atoms (say, A on the bottom layer and B on the top layer) reside on top of each

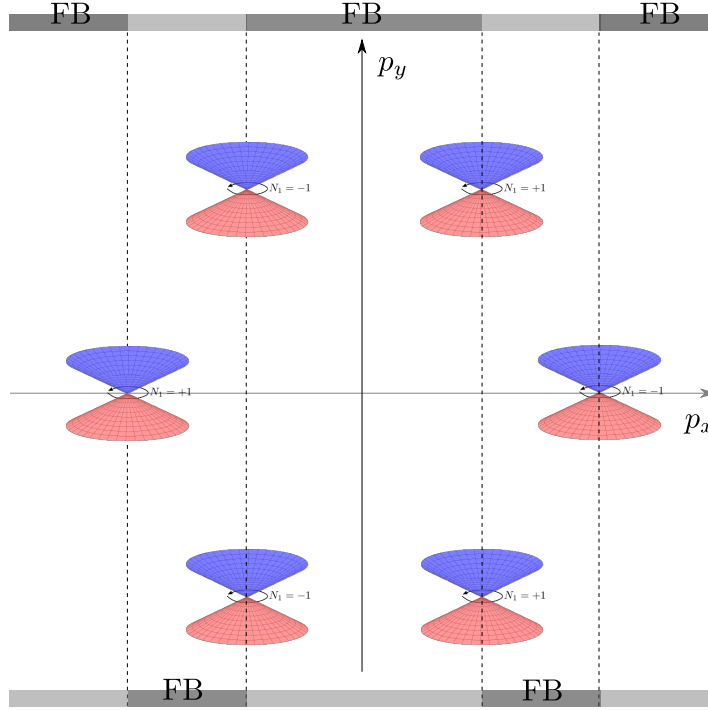


Fig. 7 Formation of a flat band in the zigzag (lower part of the figure) or bearded (upper part) edges of graphene.

other, whereas the other atom of the unit cell (B on the bottom and A on the top) are on the bottom/top of the other hexagon. Therefore, the interlayer coupling between the first pair of atoms is much stronger than the coupling between the second pair. Taking into account only this strongest coupling then produces the Hamiltonian of the form

$$H_K = \begin{pmatrix} v_F \mathbf{p} \cdot \boldsymbol{\sigma} & -\gamma_1 \sigma_{\downarrow} \\ -\gamma_1^* \sigma_{\uparrow} & v_F \mathbf{p} \cdot \boldsymbol{\sigma} \end{pmatrix} \quad (19)$$

around one of the graphene valleys (K -point) for this pair of layers. Here γ_1 quantifies the interlayer hopping. Around the other valley (K' point) the Hamiltonian is $H_{K'}(p_x, p_y) = H_K(p_x, -p_y)$. It is straightforward to show that $H_{K/K'}$ have four branches of eigenvectors, two gapped ones (with $\varepsilon(|p|=0) = \pm\gamma_1$) and two with a quadratic dispersion around a Fermi node, $\varepsilon^4 = |\gamma_1|^2 (p/p_{FB})^4$, where $p_{FB} = |\gamma_1|/v_F$. The corresponding $N_1 = 2$ (-2) for H_K ($H_{K'}$).

Beyond the bilayer, the graphene layers can be stacked in two qualitatively different ways by respecting the AB stacking for each pair of layers. In Bernal stacking, the line of strongest interlayer coupling is straight, i.e., connects the same atoms in each layer whereas for rhombohedral (ABC) stacking, it follows an armchair-type pattern, i.e., the strongly coupled atoms differ between neighbouring pairs of layers.

The corresponding elements of the momentum space Hamiltonians coupling layers n and m for 2D momenta around the K point are

$$H_{mn}^{\text{Bernal}} = v_F \mathbf{p} \cdot \boldsymbol{\sigma} \delta_{mn} - \gamma_1 \delta_{m,n+1} \{ \sigma_{\uparrow} [(-1)^m - 1] + \sigma_{\downarrow} [(-1)^m + 1] \} / 2 + \text{h.c.} \quad (20)$$

$$H_{mn}^{\text{rhombohedral}} = v_F \mathbf{p} \cdot \boldsymbol{\sigma} \delta_{mn} - \gamma_1 \delta_{m,n+1} \sigma_{\uparrow} + \text{h.c.} \quad (21)$$

In H^{Bernal} the terms in square brackets take care of indexing the even and odd layers separately. Note that since the choice of the A/B indices for the graphene sublattice atoms is arbitrary, we could have also chosen to write the coupling in $H^{\text{rhombohedral}}$ in terms of σ_{\uparrow} instead of σ_{\downarrow} . Formally, these two choices correspond to different signs of the bulk topological invariants (see below), but they have a meaning only in the presence of (Bernal) stacking faults that change the coupling around some particular interface.

3.3 Bulk Fermi line in Bernal graphite

We first derive the bulk dispersion of Bernal graphite by including only the strongest interlayer hopping term γ_1 . We make the bulk Ansatz

$$\psi_n^T = \begin{cases} \begin{pmatrix} \alpha_o & \beta_o \end{pmatrix} e^{ip_z n a / \hbar}, & n \text{ odd} \\ \begin{pmatrix} \alpha_e & \beta_e \end{pmatrix}, & n \text{ even} \end{cases} \quad (22)$$

for the wave function on the n -th layer. Here p_z is the momentum in the direction perpendicular to the layers and a is the distance between the layers. This is an eigenfunction with energy ε provided that the coefficients $\alpha_{e/o}, \beta_{e/o}$ satisfy

$$\underbrace{\begin{pmatrix} 0 & v_F p_- & 0 & -2\gamma_1 \cos(p_z a / \hbar) \\ v_F p_+ & 0 & 0 & 0 \\ 0 & 0 & 0 & v_F p_- \\ -2\gamma_1^* \cos(p_z a / \hbar) & 0 & v_F p_+ & 0 \end{pmatrix}}_{H_B} \begin{pmatrix} \alpha_o \\ \beta_o \\ \alpha_e \\ \beta_e \end{pmatrix} = \varepsilon \begin{pmatrix} \alpha_o \\ \beta_o \\ \alpha_e \\ \beta_e \end{pmatrix}, \quad (23)$$

where $p_{\pm} = p_x \pm ip_y \equiv p_{\perp} e^{i\phi}$, $p_{\perp} \geq 0$. This has (four) zero-energy solutions at $p_x = p_y = 0$, regardless of the value of p_z . Within this approximation, Bernal graphite has therefore two Dirac lines, running through the K and K' points of the 2D graphene band structure, or between the H points in the 3D graphite band structure, see Fig. 3.3. Including higher-order hopping terms in the Hamiltonian expands this line into electron and hole pockets [26]. However, let us first analyze the topology of H_B . The topological charge in this case is of the form of Eq. (17), where the contour C runs around the Dirac lines as indicated in Fig. 8, and σ_z should be

replaced by $(\sigma_z \otimes 1)$. This produces $N_1 = \pm 2$, where the factor 2 takes care of the additional layer degree of freedom in Eq. (23).

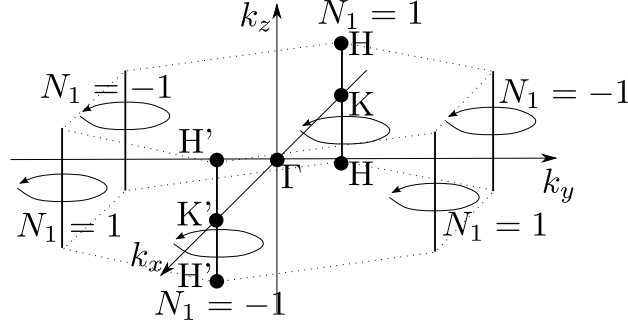


Fig. 8 Fermi lines in Bernal graphite within the nearest-neighbour interlayer approximation. This picture expands the 2D momentum space (p_x/p_y plane) of graphene to the 3D space where p_z runs between $-\hbar\pi/a$ to $\hbar\pi/a$ (a is the interlayer spacing).

This is thus nothing but the generalization of the graphene topological charge to graphite and it yields $N_1 = \pm 2$ for the momenta along the lines $H - K - H/H' - K' - H$ [26], where the $H^{(l)}$ point is shifted from the $K^{(l)}$ point in the p_z direction by $\hbar\pi/a$. Based on the bulk-boundary correspondence we may therefore expect to have surface states at the lateral boundaries of Bernal graphite, as extensions of the flat band states in zigzag graphene, but now the flat band extends throughout the first Brillouin zone in the p_z direction.

Let us now consider the effect of higher-order hopping elements. First they split the Dirac line with multiple charge $N_1 = 2$ into elementary Dirac lines. The natural splitting would be into two lines with charges $N_1 = 1$. However, the situation is more interesting, see Fig. 9 and Refs. [26, 27]. The $N_1 = 2$ line splits into 4 Dirac lines: three lines with trigonal arrangement have $N_1 = 1$, while the central line has $N_1 = -1$. The total topological invariant remains the same, $N_1 = 1 + 1 + 1 - 1 = 2$. In addition, the higher-order hoppings break the symmetry Γ [20] underlying the topological protection. Without the topological protection the four Dirac lines are expanded into four pairs of electron and hole pockets, which touch each other at four points. As a result the surface states of Bernal graphite cease to be flat on the energy scale related to those higher-order hoppings.

3.4 Spiral Fermi line in rhombohedral graphite

To obtain the bulk dispersion of rhombohedral graphite, it is enough to make the Ansatz

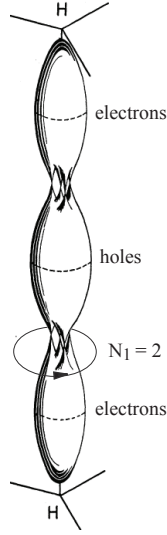


Fig. 9 Graphite Fermi surface from Ref. [26]. It consists of the electron and hole pockets connected at four points. Each point is described by topological invariant in Eq. (17): the point in the center has $N_1 = -1$ and the other three points have $N_1 = 1$. Such structure originates from the nodal line with $N_1 = 2$ in the Hamiltonian (23), when the higher order hopping elements are taken into account.

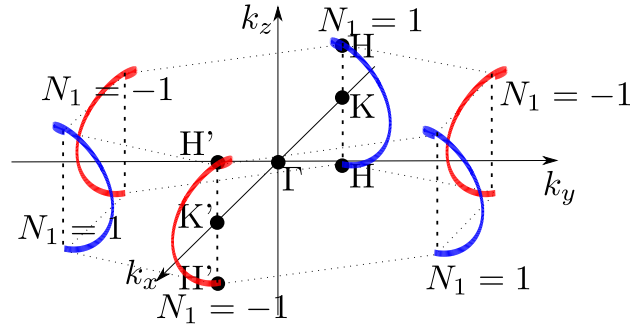


Fig. 10 Fermi spirals in rhombohedral graphite.

$$\psi_n = \begin{pmatrix} \alpha \\ \beta \end{pmatrix} e^{ip_z n a / \hbar}. \quad (24)$$

This is an eigenfunction of $H^{\text{rhombohedral}}$ if α and β satisfy

$$\underbrace{\begin{pmatrix} 0 & v_F p_- - \gamma_1 \exp(ip_z a / \hbar) \\ v_F p_+ - \gamma_1^* \exp(-ip_z a / \hbar) & 0 \end{pmatrix}}_{H_{\text{RHG}}} \begin{pmatrix} \alpha \\ \beta \end{pmatrix} = \varepsilon \begin{pmatrix} \alpha \\ \beta \end{pmatrix} \quad (25)$$

for some energy ε . The zero-energy solutions are found along a spiral in the momentum space,

$$p_z a = \arctan\left(\frac{p_y}{p_x}\right) = \phi, \quad v_F p_\perp = |\gamma_1|. \quad (26)$$

In this case the topological charge equals the spiral helicity, and can be defined by Eq. (17) where the integration contour runs over the 1st Brillouin zone ($-\pi/a$ to π/a) in the p_z -direction. For p_z running close to the line from the H point via K back to H, $N_1 = 1$ whenever the transverse momentum $p_x \pm ip_y$ is inside the spiral, i.e., $p_\perp < |\gamma_1|/v_F$. For larger momenta away from the $H - K - H$ line, $N_1 = 0$. On the other hand, for the path $H' - K' - H'$ the spiral is defined by Eq. (26), where $p_y \leftrightarrow -p_y$, inverting the helicity and the sign of N_1 to -1.

As a result of the existence of the non-trivial topological charge, the surface layers of rhombohedral graphite contain flat bands, i.e., $\varepsilon(p_\perp < |\gamma_1|/v_F) = 0$. This can be understood as follows. For each \mathbf{p}_\perp with $p_\perp \neq |\gamma_1|/v_F$, the Hamiltonian $H_{\mathbf{p}_\perp}(p_z)$ describes a 1D insulator. For $p_\perp < |\gamma_1|/v_F$, this insulator is topological, since it has the topological charge $N_1(\mathbf{p}_\perp) = 1$. According to the bulk-boundary correspondence, each topological insulator has an edge state with zero energy. These states form a flat band in the region $p_\perp < |\gamma_1|/v_F$.

4 Flat band at strained interfaces

Recently another possible source of the topological flat band has been discussed in two materials: highly oriented pyrolytic Bernal graphite (HOPG) [28] and heterostructures SnTe/PbTe, PbTe/PbS, PbTe/PbSe, and PbTe/YbS consisting of a topological crystalline insulator and a trivial insulator [29]. In both cases the flat band comes from a misfit dislocation array, which is spontaneously formed at the interface between two crystals due to the lattice mismatch. In Ref. [28] the lattice of screw dislocations has been considered, which emerges at the interface between two domains of HOPG with different orientations of crystal axes. In Ref. [29] the misfit dislocation array is formed at the interface between topological and trivial insulators.

The above two systems exhibit similar phenomenon. In both cases superconductivity related with the interfaces has been found [30, 31]. The reported transition temperature essentially exceeds the typical transition temperature expected for the bulk materials. A possible origin of this phenomenon is the flat band at the interfaces, where the transition temperature could be proportional to the coupling constant and the area of the flat band.

The topological origin of the flat bands in these systems can be understood either in terms of the overlapping of the 1D flat bands formed within the dislocations or using the following consideration. In case of the heterostructures, on one side of the interface the insulator is topological, and thus the interface contains Dirac fermions. The strain at the interface (with its dislocations) acts on Dirac fermions as the effective magnetic field. Such emergent field is now extensively discussed for

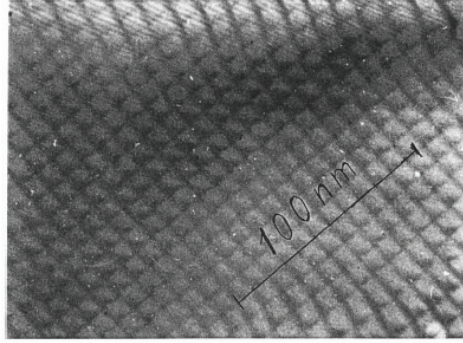


Fig. 11 Misfit dislocation grid at the interface from [N. Ya. Fogel, Phys. Rev. B **66**, 174513 (2002)] [30].

strained graphene, see e.g. the most recent paper Ref. [32] and references therein. The effective magnetic field B produces the required flat band, since the first Landau level for massless Dirac fermions has zero energy. When the period decreases, the field B increases, giving rise to enhanced density of states, which is proportional to B . This is equivalent to increase of the area of flat band in the scenario discussed in Sec. 3. Such increase of transition temperature is discussed in Ref. [29].

In particular, Ref. [29] considered the case where the massless Dirac Hamiltonian of the topological insulator experience a periodic field. They arrived at the Hamiltonian of the form

$$H_{TF} = -i\partial_x \sigma_x + [k_y - A(x)] \sigma_y, \quad (27)$$

written in terms of (scaled) momentum k_y along the dislocation, and a scaled strain-induced gauge field $A(x)$ satisfying $A(x+d) = A(x)$ and $\int_0^d A(x) dx = 0$. In the case of Ref. [29], $A(x) = \beta \cos(2\pi x/d)$, but the approach works for a more general periodic vector potential as well. Due to the position dependent vector potential, there is no translation symmetry in the x direction and the momentum in the x -direction is not a good quantum number. However, due to the periodicity of the potential we can use Bloch's theorem and define the pseudomomentum \tilde{k}_x . This allows for calculating the spectrum of Eq. (27), plotted in Fig. 12 and exhibiting (an approximate) flat band for $k_y < \beta/2$ and for all values of $k_x \in [-\pi/d, \pi/d]$.

The emergence of the approximate flat band in Eq. (27) can be understood by first considering the case $k_y = 0$. In that case the Hamiltonian has two (unnormalized) zero-energy solutions,

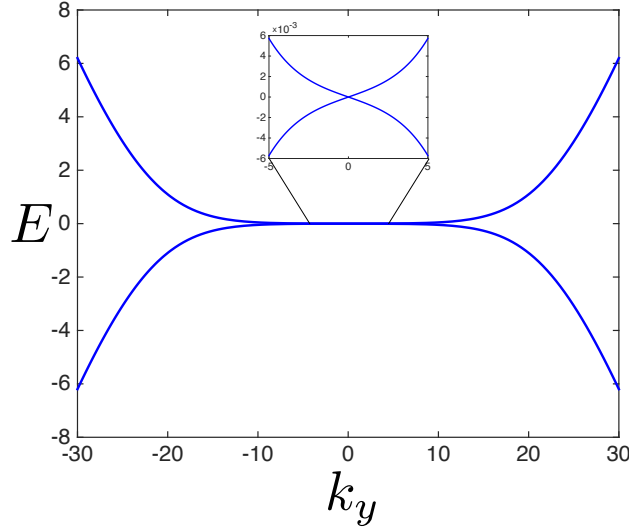


Fig. 12 Spectrum of Eq. (27) with $\beta = 30$. Inset shows the (approximate) linear dispersion with low values of k_y , and with a speed as in Eq. (4).

$$\begin{aligned}\psi_+ &= \begin{pmatrix} 0 \\ 1 \end{pmatrix} \exp\left[\int_0^x A(x') dx'\right] \\ \psi_- &= \begin{pmatrix} 1 \\ 0 \end{pmatrix} \exp\left[-\int_0^x A(x') dx'\right].\end{aligned}$$

Let us include the term $H_1 = k_y \sigma_y$ as a perturbation. The second order secular equation produces the 2×2 Hamiltonian constructed from the matrix elements of the Hamiltonian H_1 :

$$\begin{pmatrix} 0 & H_{+-}^{(1)} \\ H_{-+}^{(1)} & 0 \end{pmatrix} = c \begin{pmatrix} 0 & k_y \\ k_y & 0 \end{pmatrix}$$

with the spectrum $E = \pm ck_y$. The slope c of the spectrum is obtained from the matrix elements of the normalized eigenfunctions

$$c = \frac{\int_{-\infty}^{\infty} dx \psi_+ \psi_-}{\int_{-\infty}^{\infty} dx \exp\left[2 \int_0^x A(x') dx'\right]} = \frac{d}{\int_0^d e^{2 \int_0^x A(x') dx'} dx}.$$

For $A(x) = \beta \cos(x)$ we thus get $c = 1/I_0(2\beta)$, where $I_0(x)$ is the zeroth Bessel function of the first kind. When $c \ll 1$, requiring $\beta \gg 1$, the result is an approximate flat band.

Alternatively, we may consider the case of a periodic line dislocation. There, the vector potential is proportional to the strain field, $A(x) = \alpha_1 u_{xx}(x) + \alpha_2 u_{yy}(x)$, where α_1 and α_2 are coupling constants and

$$u_{xx}(x) = \frac{bz}{2\pi(1-\nu)} \frac{3x^2 + z^2}{(x^2 + z^2)^2}$$

$$u_{yy}(x) = \frac{bz\nu}{\pi(1-\nu)} \frac{1}{x^2 + z^2},$$

where b is the size of the Burgers vector of the dislocation, z is the distance from the dislocation plane, and ν is the Poisson ratio. We also assume that such dislocations repeat after each d . In this case we may estimate the slope c for $d \gg z$ by

$$c \approx \exp \left[-2 \int_0^\infty A(x) \right] = \exp \left[-\frac{b(\alpha_1 + \nu\alpha_2)}{1-\nu} \right].$$

The flat band dispersion where $c \ll 1$ thus requires either $\nu \approx 1$ or coupling constants $\alpha_i \gg 1/b$. Note that this result shows that the estimates done in Ref. [29] are overoptimistic, as there $\alpha b \approx 1$.

5 Superconductivity in graphene or graphite?

As discussed in Sec. 3, bulk neutral graphite and graphene are typically considered to have a very low density of states. This is why the occurrence of superconductivity in these bulk systems would require a strong doping, shifting the Fermi energy to a finite value and thereby increasing the density of states. Let us consider the example case of a 2D Fermi line with the superconducting coupling g , but with a shifted Fermi level by a value μ . In this case Eq. (3) yields for $\mu = 0$ [33]

$$\Delta = (a\varepsilon_{uv} - 1/a)/2 > 0, \quad (28)$$

where $a = g/(\pi\hbar^2 v_F^2)$. This is non-zero only for a large coupling strength $a > 1/\varepsilon_{uv}$. For weak coupling $|a| < 1/\xi_c$, superconductivity is enhanced by doping, because for non-zero μ the solution is $\Delta = 2|\mu| \exp(-\frac{1/a - \xi_c}{|\mu|} - 1)$.

This strategy has been followed by some graphite experimentalists. For example Ref. [34] demonstrates bulk superconductivity of two graphite intercalation compounds C_6Yb and C_6Ca with critical temperatures of 6.5 and 11.5 K, respectively. There one of the effects from the intercalant layers is the charge transfer, i.e., doping the graphite.

The situation is opposite in flat band systems: doping does not aid superconductivity, but rather decreases the critical temperature. With a non-zero chemical potential μ , the gap becomes

$$\Delta = \sqrt{\Delta_{FB}^2 - \mu^2}, \quad (29)$$

where Δ_{FB} is the gap obtained for $\mu = 0$, as in Eq. (7).

There are experimental indications for the presence of superconductivity at graphite interfaces [31]. In this case, the interfaces form between differently oriented regions of Bernal graphite, so that the graphite c -axis (p_z in our work here) runs perpendicular to these surfaces. These observations hence cannot be explained by the flat bands at the lateral interfaces (along p_x or p_y) as one would expect in Bernal graphite. There are also no direct indications of the presence of rhombohedral stacking in these systems, but the resolution of the imaging does not allow ruling out some rhombohedral regions close to the interfaces exhibiting superconducting properties. Note that rhombohedral stacking has been found in highly oriented pyrolytic graphite, see for example [35, 36]. The remaining scenario is based on the formation of an array of dislocations (Sec. 4) at these surfaces as the surface layers try to adapt to the neighbouring graphite planes.

The discussion in Sec. 1 concerns only the relation of the mean field order parameter with normal-state electronic spectrum. The details of the flat band superconducting state, such as the quasiparticle spectrum, supercurrent and collective modes, depend on the way the flat band is formed. The case of rhombohedral graphite has been worked out in Refs. [37, 38, 39] and summarized in [40]. The density of states in the superconducting state was computed in [41]. In that case the superconducting spectrum is not flat, but rather has an inverse parabolic shape and exhibits a minigap whose value is inversely proportional to the distance between adjacent surfaces. The supercurrent is characterized by a large critical current that is linearly proportional to Δ . However, in this model the supercurrent does not only flow along the surfaces, but also between them. On the other hand it is clear that not all types of flat bands can describe a state with a non-vanishing critical current. For example, an entirely isolated region in momentum space having a flat band describes a set of completely localized electrons, which cannot be made to carry supercurrent.

In this chapter we have concentrated on illustrating the results for mean-field models of superconductivity on flat bands. As discussed in [40], fluctuation effects are much more important in flat band superconductors than in ordinary BCS superconductors. The nature of the fluctuation response depends on the mechanism of the flat band formation, and the ensuing superconducting spectrum. The details of such fluctuation effects we leave for further work.

As we have discussed in this chapter, there are many ways of realizing (approximate) flat bands. Some of these realizations may be relevant in interfaces of graphite, where indications of superconductivity with a very high critical temperature have been observed. It remains to be demonstrated whether these properties can be explained within the flat band scenario of superconductivity.

We acknowledge Pablo Esquinazi, Ville Kaupilla and Timo Hyart for discussions. This work was supported by the Academy of Finland through its Center of Excellence program, and by the European Research Council (Grant No. 240362-Heatronics).

References

1. Y. Kopaev, Superconductivity of alloyed semimetals, *JETP* **31**, 544 (1970).
2. Y. Kopaev and A. Rusinov, Enhancement of superconducting critical temperature due to metal-semiconductor transition, *Phys. Lett. A* **121**, 300 (1987).
3. V.A. Khodel and V.R. Shaginyan, Superfluidity in system with fermion condensate, *JETP Lett.* **51**, 553 (1990).
4. G.E. Volovik, A new class of normal Fermi liquids, *JETP Lett.* **53**, 222 (1991).
5. P. Nozieres, Properties of Fermi liquids with a finite range interaction, *J. Phys. (Fr.)* **2**, 443–458 (1992).
6. A.A. Shashkin, V.T. Dolgoplov, J.W. Clark, V.R. Shaginyan, M.V. Zverev and V.A. Khodel, Merging of Landau levels in a strongly-interacting two-dimensional electron system in silicon, *Phys. Rev. Lett.* **112**, 186402 (2014).
7. G.E. Volovik, On Fermi condensate: near the saddle point and within the vortex core, *JETP Lett.* **59**, 830–835 (1994).
8. D. Yudin, D. Hirschmeier, H. Hafermann, O. Eriksson, A.I. Lichtenstein and M.I. Katsnelson, Fermi condensation near van Hove singularities within the Hubbard model on the triangular lattice, *Phys. Rev. Lett.* **112**, 070403 (2014).
9. L. Landau, Paramagnetism of metals, *Z. Phys.* **64**, 629–637 (1930).
10. S. Ryu and Y. Hatsugai, Topological origin of zero-energy edge states in particle-hole symmetric systems, *Phys. Rev. Lett.* **89**, 077002 (2002).
11. T.T. Heikkilä, N.B. Kopnin and G.E. Volovik, Flat bands in topological media, *JETP Lett.* **94**, 233–239 (2011); arXiv:1012.0905.
12. A.P. Schnyder and S. Ryu, Topological phases and flat surface bands in superconductors without inversion symmetry, *Phys. Rev. B* **84**, 060504(R) (2011).
13. G.E. Volovik, Quantum phase transitions from topology in momentum space, *Lect. Notes Phys.* **718**, 31–73 (2007).
14. R.S.K. Mong and V. Shivamoggi, Edge states and the bulk-boundary correspondence in Dirac Hamiltonians, *Phys. Rev. B* **83**, 125109 (2011).
15. A.M. Essin and V. Gurarie, Bulk-boundary correspondence of topological insulators from their respective Green's functions, *Phys. Rev. B* **84**, 125132 (2011).
16. G. M. Graf and M. Porta, Bulk-edge correspondence for two-dimensional topological insulators, *Commun. Math. Phys.* **324**, 851 (2013).
17. G.E. Volovik, *The Universe in a Helium Droplet* (Oxford University Press, Oxford, UK, 2003).
18. A.A. Burkov and L. Balents, Weyl semimetal in a topological insulator multilayer, *Phys. Rev. Lett.* **107**, 127205 (2011); A.A. Burkov, M.D. Hook, L. Balents, Topological nodal semimetals,
19. M.A. Silaev, G.E. Volovik, Andreev-Majorana bound states in superfluids, *JETP* **119**, 1042–1057 (2014),
20. T.T. Heikkilä and G.E. Volovik, Dimensional crossover in topological matter: Evolution of the multiple Dirac point in the layered system to the flat band on the surface, *JETP Lett.* **93**, 59–65 (2011).
21. Hongming Weng, Yunye Liang, Qiunan Xu, Yu Rui, Zhong Fang, Xi Dai, Yoshiyuki Kawazoe, Topological Node-Line Semimetal in Three Dimensional Graphene Networks, arXiv:1411.2175.
22. Youngkuk Kim, B. J. Wieder, C. L. Kane, A. M. Rappe, Dirac line nodes in inversion symmetric crystals, arXiv:1504.03807
23. T.T. Heikkilä, *The Physics of Nanoelectronics*, (Oxford University Press, Oxford, 2013).
24. M.I. Katsnelson, *Graphene - Carbon in Two Dimensions*, (Cambridge University Press, Cambridge, 2012).
25. P. Delplace, D. Ullmo and G. Montambaux, Zak phase and the existence of edge states in graphene, *Phys. Rev. B* **84**, 195452 (2011).

26. J.W. McClure, Band structure of graphite and de Haas-van Alphen effect, *Phys. Rev.* **108**, 612-618 (1957).
27. G.P. Mikitik and Yu.V. Sharlai, The Berry phase in graphene and graphite multilayers, *Fizika Nizkikh Temperatur*, **34**, 1012–1019 (2008).
28. P. Esquinazi, T.T. Heikkilä, Y.V. Lysogorskiy, D.A. Tayurskii, G.E. Volovik, On the superconductivity of graphite interfaces, *Pis'ma ZhETF* **100**, 374–378 (2014); arXiv:1407.2060.
29. E. Tang and L. Fu, Strain-induced partially flat band, helical snake states, and interface superconductivity in topological crystalline insulators, *Nature Phys.* **10**, 964–969 (2014); arXiv:1403.7523.
30. N. Ya. Fogel, E. I. Buchstab, Yu. V. Bomze, O. I. Yuzepovich, A. Yu. Sipatov, E. A. Pashitskii, A. Danilov, V. Langer, R. I. Shekhter, and M. Jonson, Interfacial superconductivity in semiconducting monochalcogenide superlattices, *Phys. Rev. B* **66**, 174513 (2002).
31. P. Esquinazi, Graphite and its hidden superconductivity, *Papers in Physics* **5**, 050007 (2013); A. Ballestar, J. Barzola-Quiquia, T. Scheike, and P. Esquinazi, Josephson-coupled superconducting regions embedded at the interfaces of highly oriented pyrolytic graphite, *New J. Phys.* **15**, 023024 (2013); A. Ballestar, T.T. Heikkilä, and P. Esquinazi, Interface size dependence of the Josephson critical behaviour in pyrolytic graphite, *Supercond Sci. Technol.* **27**, 115014 (2014)
32. G.E. Volovik and M.A. Zubkov, Emergent geometry experienced by fermions in graphene in the presence of dislocations, arXiv:1412.2683.
33. N.B. Kopnin and E.B. Sonin, BCS Superconductivity of Dirac electrons in graphene layers, *Phys. Rev. Lett.* **100**, 246808 (2008).
34. T.E. Weller, M. Ellerby, S.S. Saxena, R.P. Smith, and N.T. Skipper, Superconductivity in the intercalated graphite compounds C_6Yb and C_6Ca , *Nature Phys.* **1**, 39 (2005).
35. Q. Lin, T.Li, Z. Liu, Y. Song, L. He, Z. Hu, Q. Guo, and H. Ye, High-resolution TEM observations of isolated rhombohedral crystallites in graphite blocks, *Carbon* **50**, 2369 (2012).
36. S. Hattendorf, A. Georgi, M. Liebmann, and M. Morgenstern, Networks of ABA and ABC stacked graphene on mica observed by scanning tunneling microscopy, *Surf. Sci.* **610**, 53 (2013).
37. N.B. Kopnin, T.T. Heikkilä, and G.E. Volovik, High-temperature surface superconductivity in topological flat-band systems, *Phys. Rev. B* **83**, 220503(R) (2011).
38. N.B. Kopnin, Surface superconductivity in multilayered rhombohedral graphene: supercurrent, *JETP Lett.* **94**, 81 (2011).
39. N.B. Kopnin, M. Ijäs, A. Harju, and T.T. Heikkilä, High-temperature surface superconductivity in rhombohedral graphite, *Phys. Rev. B* **87**, 140503(R) (2013).
40. N.B. Kopnin and T.T. Heikkilä, Surface superconductivity in rhombohedral graphite, Ch. 9 in *Carbon-based superconductors*, edited by Junji Haruyama (Pan Stanford 2014), also at arXiv:1210.7075.
41. W.A. Muñoz, L. Covaci, and F.M. Peeters, Tight-binding description of intrinsic superconducting correlations in multilayer graphene, *Phys. Rev. B* **87**, 134509 (2013).